Crumbling Reefs and Cold-Water Coral Habitat Loss in a Future Ocean: Evidence of "Coralporosis" as an Indicator of Habitat Integrity

Sebastian J. Hennige[1]*[†], Uwe Wolfram[2]*[†], Leslie Wickes[3,4,5†], Fiona Murray[1],
J. Murray Roberts[1], Nicholas A. Kamenos[6], Sebastian Schofield[2], Alexander Groetsch[2],
Ewa M. Spiesz[7], Marie-Eve Aubin-Tam[7] and Peter J. Etnoyer[4,5]

[1] Changing Oceans Research Group, School of GeoSciences, University of Edinburgh, Edinburgh, United Kingdom, [2] School of Engineering and Physical Sciences, Heriot-Watt University, Edinburgh, United Kingdom, [3] Thrive Blue Consulting, Charleston, SC, United States, [4] Grice Marine Laboratory, College of Charleston, Charleston, SC, United States, [5] National Oceanic and Atmospheric Administration, National Centers for Coastal Ocean Science, Charleston, SC, United States, [6] School of Geographical and Earth Sciences, University of Glasgow, Glasgow, United Kingdom, [7] Department of Bionanoscience, Kavli Institute of Nanoscience, Delft University of Technology, Delft, Netherlands

Ocean acidification is a threat to the net growth of tropical and deep-sea coral reefs, due to gradual changes in the balance between reef growth and loss processes. Here we go beyond identification of coral dissolution induced by ocean acidification and identify a mechanism that will lead to a loss of habitat in cold-water coral reef habitats on an ecosystem-scale. To quantify this, we present *in situ* and year-long laboratory evidence detailing the type of habitat shift that can be expected (*in situ* evidence), the mechanisms underlying this (*in situ* and laboratory evidence), and the timescale within which the process begins (laboratory evidence). Through application of engineering principals, we detail how increased porosity in structurally critical sections of coral framework will lead to crumbling of load-bearing material, and a potential collapse and loss of complexity of the larger habitat. Importantly, *in situ* evidence highlights that cold-water corals can survive beneath the aragonite saturation horizon, but in a fundamentally different way to what is currently considered a biogenic cold-water coral reef, with a loss of the majority of reef habitat. The shift from a habitat with high 3-dimensional complexity provided by both live and dead coral framework, to a habitat restricted primarily to live coral colonies with lower 3-dimensional complexity represents the main threat to cold-water coral reefs of the future and the biodiversity they support. Ocean acidification can cause ecosystem-scale habitat loss for the majority of cold-water coral reefs.

Keywords: deep-sea coral, ocean acidification, coral, habitat loss and degradation, *Lophelia pertusa*, dissolution

INTRODUCTION

Ocean acidification is of concern to both tropical and cold-water coral (CWC) reefs (Secretariat of the Convention on Biological Diversity [CBD], 2014). It can cause a reduction in the growth rate of live coral (Kline et al., 2019), and dissolution of dead coral skeletons (skeletons no longer covered in soft tissue) either directly (Hennige et al., 2015a) or indirectly through increasing rates of bioerosion

(Wisshak et al., 2012; Davidson et al., 2018). This can lead to a reduction in the net growth rate in the case of tropical coral reefs (Albright et al., 2018; Eyre et al., 2018; Kline et al., 2019). For CWC reefs, the severity of the threat of ocean acidification is vastly different to that projected for tropical reefs due to two factors: (1) CWC reef habitats and the biodiversity provision afforded by them is mostly provided by dead coral skeletal framework and exposed rubble ("live" coral has soft-tissue covering the skeleton whilst "dead" coral is when soft-tissue is no longer present, and the skeleton is exposed to seawater). (2) The aragonite saturation horizon (ASH), which is the depth at which aragonite (the polymorph of calcium carbonate commonly precipitated by scleractinian corals) becomes undersaturated, will rise above the majority of CWC reefs over the coming decades. Ocean acidification can thus have a *direct* and potentially rapid impact on the major load-bearing fraction of these habitats; the dead coral skeletons.

While tropical reefs are projected to experience reduced aragonite saturation levels in addition to large diel fluctuations from biological activity (Shaw et al., 2012), they will not be exposed to seawater that is permanently undersaturated with respect to aragonite ($\Omega_{Arag} < 1$), unlike the majority of CWC reefs. CWCs are typically restricted to oceanic waters and temperatures between 4°C and 12°C, which is ~50–1000 m at high latitudes, and down to 4000 m beneath warm water masses at low latitudes (Roberts et al., 2006). The reefs and carbonate mounds they form can be up to 300 m high, several kilometres in diameter (Roberts et al., 2006), and have a global distribution (Freiwald et al., 2005). Projected ocean acidification due to rising atmospheric concentrations of CO_2 (Secretariat of the Convention on Biological Diversity [CBD], 2014) will drive the ASH shallower (Perez et al., 2018), leaving ~70% of these CWC reefs in permanently aragonite undersaturated water by the end of the century (year 2099 with CO_2 concentrations of 788 ppmv) (Guinotte et al., 2006).
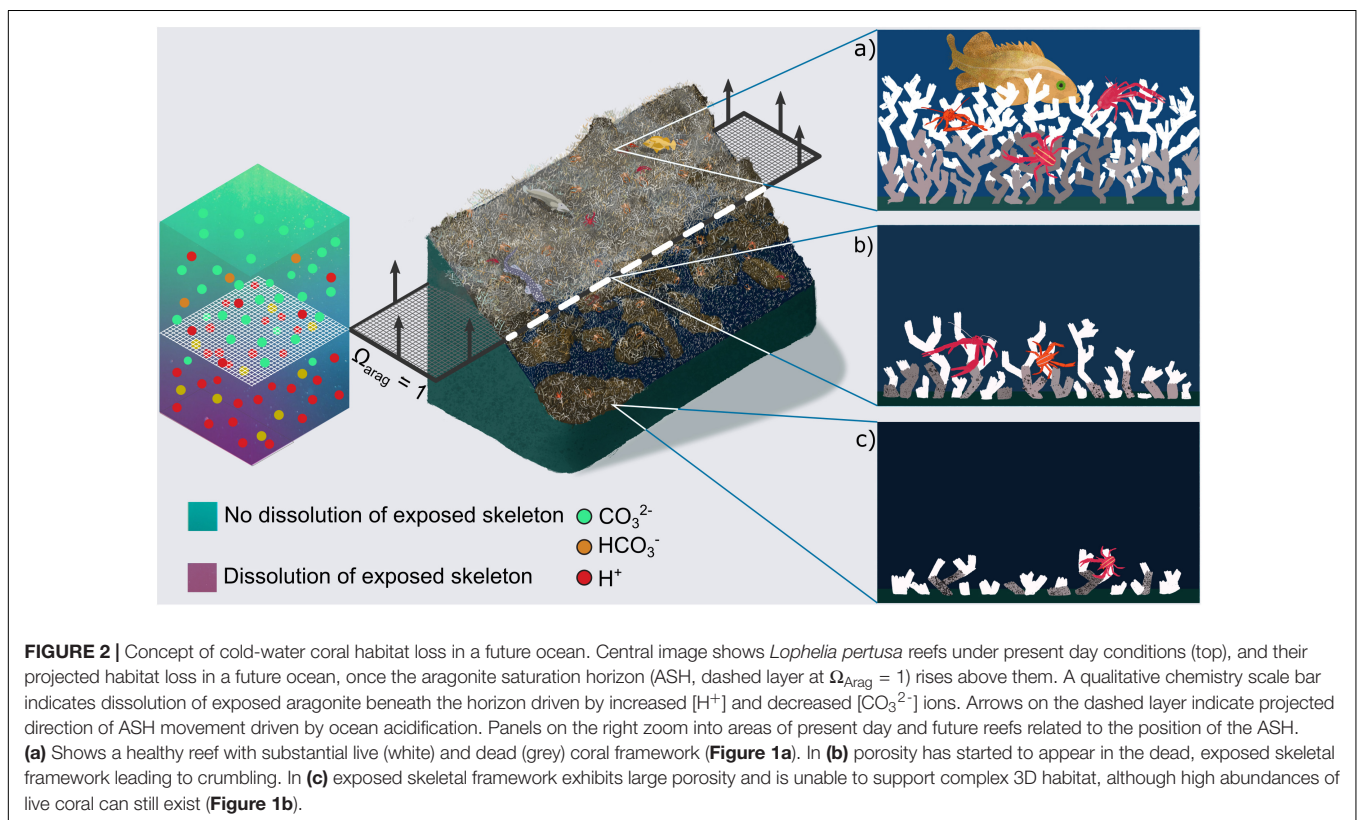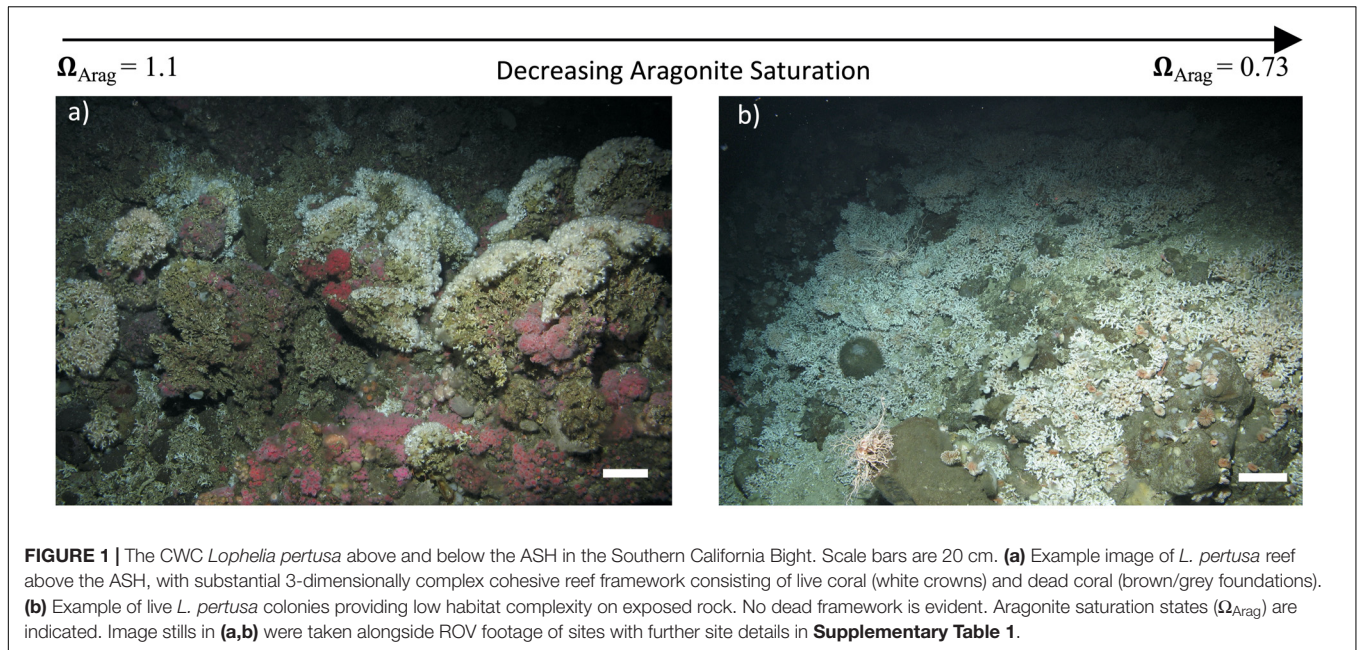
The particular concern is whether CWC reef habitat will persist once the ASH shoals past them, given that the majority of these reefs are currently above the ASH (over 95% in pre-industrial times; Guinotte et al., 2006). This leaves us with the question of whether CWC reef habitat will persist once the ASH shoals past them. One possibility is that gradual dissolution of exposed skeletal material (when exposed to aragonite undersaturation) could be countered by sustained live coral growth rates and sediment infilling, meaning little difference to reef structures. Conversely, dissolution of the supporting, dead coral framework that sits above infilled sediment/rubble and below live coral could lead to a rapid degradation of habitats and a dramatic loss in habitat complexity if it occurs faster than sediment infilling. To understand what future impacts of a shoaling ASH may be, it is crucial that we look at current CWC reefs that are found below the ASH (Thresher et al., 2011; Baco et al., 2017).

While the vast majority of cold-water reefs occur in the North Atlantic where the ASH can extend to ~2000 m, small patchy reefs do exist in the North Pacific (Hardin et al., 1994; Baco et al., 2017; Gómez et al., 2018; Salgado et al., 2018) where the ASH occurs at depths from ~50 to 600 m.

This shallow ASH is a consequence of global thermohaline circulation (Feely et al., 2004), anthropogenic input of carbon dioxide (Feely et al., 2008), and regional upwelling of CO_2-rich older water masses onto the continental shelf (Feely et al., 2008). Pacific localities, like the Southern California Bight, are projected to experience rapid shoaling of the ASH (Gruber et al., 2012; Hauri et al., 2013; Osborne et al., 2019), meaning corals in these systems are at the forefront of environmental change. CWC in these localities are currently in conditions that are analogous to the water chemistry that most CWC reefs will experience by the year 2099 (Guinotte et al., 2006). Therefore, the Southern California Bight provides a "natural laboratory" for assessing projected impacts of ocean acidification on CWC ecosystems.

When we look at coral habitats in the Southern Californian Bight (**Figure 1**), it is clear that there is a shift between the *L. pertusa* habitats above and below the ASH, with a marked absence of dead coral and low habitat complexity in habitats below the ASH (**Figure 1b**). The occurrence of live coral below the ASH in general complements research on *L. pertusa* to date, indicating that live coral can continue to calcify under projected temperature and ocean acidification conditions (McCulloch et al., 2012a,b; Hennige et al., 2014b, 2015a; Lunden et al., 2014; Movilla et al., 2014). However, whether the acclimatory cost of this can be met in the long-term is still debatable, with different laboratory studies highlighting different processes depending on time scales of the experiments, energetic input, presence of additional stressors or species of framework forming CWC (Hennige et al., 2015a; Büscher et al., 2017; Gammon et al., 2018).
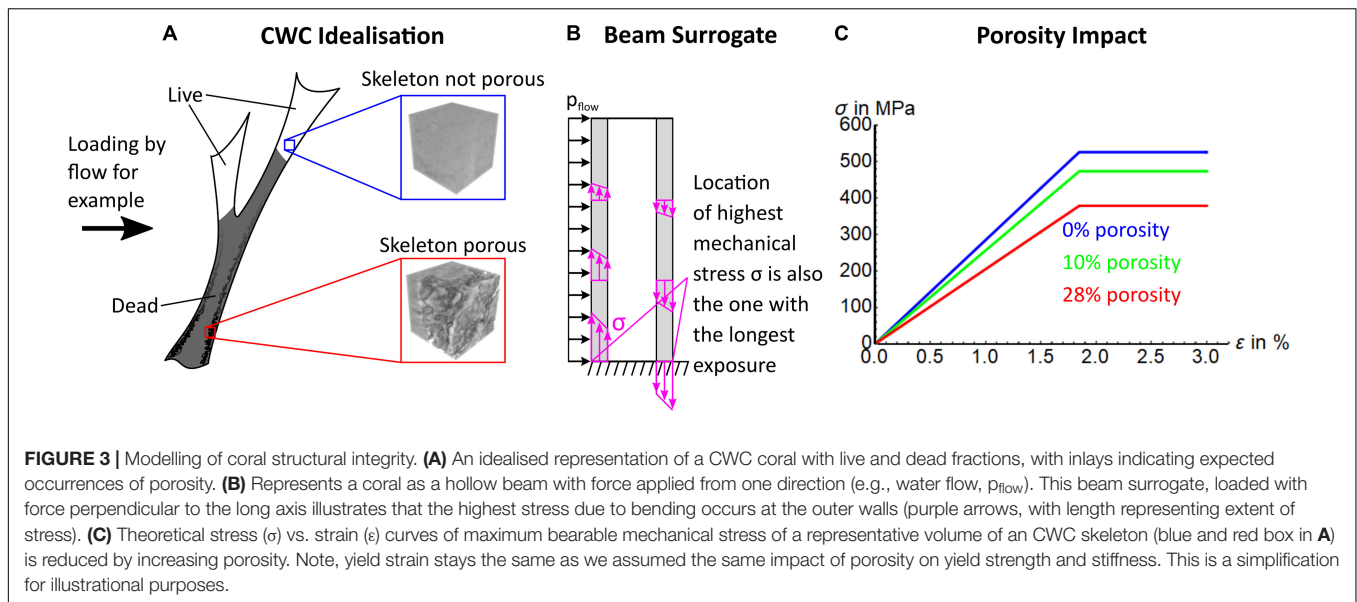
Regardless, focus on just live corals ignores the larger and more serious ecosystem-scale threat to these habitats and associated biodiversity from a shoaling ASH; the potentially rapid loss of structural integrity and habitat complexity (**Figure 2**). This is of particular concern as high biodiversity associated with CWC reefs is strongly related to their structural complexity (Henry and Roberts, 2007, 2015; Kazanidis et al., 2015). The majority of a CWC habitat is typically exposed dead coral (Vad et al., 2017) sitting on top of solid substrate or consolidated sediment and rubble, with the living coral concentrated at the outermost parts of the reef above the dead coral, where the coral can access and capture passing prey (Roberts et al., 2006, 2009). The complexity of CWC reefs not only sustains locally high species diversity (alpha diversity) but the hydrodynamic regimes and spatial mosaic of macro- and micro-habitats within the reefs also drives high species turnover (beta diversity) (Henry and Roberts, 2007, 2015). Interweaving coral branches create many small cavities for fish and invertebrates (e.g., **Figure 1a**) and provide important refuge and spawning sites for vulnerable low fecundity fish, including deep-water sharks (Henry et al., 2013). Furthermore, coral framework baffles mobile sediment leading over time to substantial deep-water coral reef and coral carbonate mound development (Roberts et al., 2006). The ability of dead coral framework to support living colonies by sustaining external loads is therefore of paramount importance not only for CWC habitat complexity and its ability to support other species, but also for reef and mound formation.

FIGURE 1 | The CWC *Lophelia pertusa* above and below the ASH in the Southern California Bight. Scale bars are 20 cm. **(a)** Example image of *L. pertusa* reef above the ASH, with substantial 3-dimensionally complex cohesive reef framework consisting of live coral (white crowns) and dead coral (brown/grey foundations). **(b)** Example of live *L. pertusa* colonies providing low habitat complexity on exposed rock. No dead framework is evident. Aragonite saturation states (Ω_{Arag}) are indicated. Image stills in **(a,b)** were taken alongside ROV footage of sites with further site details in **Supplementary Table 1**.

FIGURE 2 | Concept of cold-water coral habitat loss in a future ocean. Central image shows *Lophelia pertusa* reefs under present day conditions (top), and their projected habitat loss in a future ocean, once the aragonite saturation horizon (ASH, dashed layer at $\Omega_{Arag} = 1$) rises above them. A qualitative chemistry scale bar indicates dissolution of exposed aragonite beneath the horizon driven by increased [H^+] and decreased [CO_3^{2-}] ions. Arrows on the dashed layer indicate projected direction of ASH movement driven by ocean acidification. Panels on the right zoom into areas of present day and future reefs related to the position of the ASH. **(a)** Shows a healthy reef with substantial live (white) and dead (grey) coral framework (**Figure 1a**). In **(b)** porosity has started to appear in the dead, exposed skeletal framework leading to crumbling. In **(c)** exposed skeletal framework exhibits large porosity and is unable to support complex 3D habitat, although high abundances of live coral can still exist (**Figure 1b**).

The Underlying Mechanism

To understand how a 3-dimensionally complex *L. pertusa* reef can shift to become a habitat with low complexity and low biodiversity support (**Figures 1, 2**), we need to consider the stability of live and dead coral in a way that is scalable to larger reef framework. For this, we model dissolution (resulting in an increase of skeletal porosity) in a coral (**Figure 3A**) simplified as a hollow beam fixed at its base with a load (e.g., water current) applied from the side (**Figure 3B**). Such a construct is reproducible and scalable from a single coral branch to a complex 3-Dimensional framework through computational and mathematical modelling (**Supplementary Figure 8**). In a hollow

FIGURE 3 | Modelling of coral structural integrity. **(A)** An idealised representation of a CWC coral with live and dead fractions, with inlays indicating expected occurrences of porosity. **(B)** Represents a coral as a hollow beam with force applied from one direction (e.g., water flow, p$_{flow}$). This beam surrogate, loaded with force perpendicular to the long axis illustrates that the highest stress due to bending occurs at the outer walls (purple arrows, with length representing extent of stress). **(C)** Theoretical stress (σ) vs. strain (ε) curves of maximum bearable mechanical stress of a representative volume of an CWC skeleton (blue and red box in **A**) is reduced by increasing porosity. Note, yield strain stays the same as we assumed the same impact of porosity on yield strength and stiffness. This is a simplification for illustrational purposes.

beam coral surrogate, the critical point of failure (represented by greatest length of stress arrow (σ) in **Figure 3B**) is located at the outer surface at the base. Loss of material by increasing porosity specifically in those locations increases the fragility of the whole structure at its weakest point, leading to early onset of mechanical failure (crumbling and collapse) of the foundation framework within reef structures. Stress under the same applied load will always be higher toward the fixed base of a beam (**Figure 3B**), which is also the site of the oldest material, potentially subjected to dissolution for the longest time. Stress (σ) vs. strain (ε) curves of a representative volume element of coral skeleton demonstrates that such an increase in porosity in the skeleton leads to a decrease in apparent skeleton stiffness (initial slope) and maximum bearable mechanical stress (flat part of σ vs. ε curves, **Figure 3C**), equating to reduced stiffness and strength of the coral wall and, thus, the whole sample. The result of this process is observed in *in situ* reefs living below the ASH with little or no dead reef framework and only low structural height of living coral (**Figure 1**). The exact timescale when this becomes critical for 3D reef framework relative to exposure intensity and duration is yet to be determined, and here we present the progression of this process from *in situ* and long-term mesocosm experiments.

MATERIALS AND METHODS

Methods below describe the collection of *in situ* data, treatments of experimentally incubated corals, and material analysis of both *in situ* and experimental corals. *In situ* sampling included coral collection, water chemistry and habitat video analysis. Analysis of the skeletons includes: synchrotron radiation computed tomography for high resolution imagery; Raman imaging and X-ray diffraction for biomineralisation; skeletal density; nanoindentation to determine stiffness and hardness of materials; and using a simple 1D constitutive model to examine the effects of porosity.

Submersible Surveys

National Oceanic and Atmospheric Administration's (NOAA's) National Marine Fisheries Service (NMFS) Southwest Fisheries Science Centers (SWFSC) has conducted hundreds of remotely operated vehicle (ROV) surveys throughout the Southern California Bight since 2000. SWFSC Fishery Resource Division (FRD) conducted most of these dives using an ROV, the Phantom DS4 ROV (Deep Ocean Engineering, Inc.), equipped with a forward-looking video camera and high-resolution still camera (Scorpio, Insite Pacific). Dives in 2012 employed the HDHV ROV, equipped with high-definition video and still cameras. Dives from 2003 to 2012 (*n* = 570) were evaluated for *L. pertusa* presence using photographs and video. Many other surveys were conducted by SWFSC Fisheries Ecology Division (FED) using the human occupied research submersible Delta. The submersible dives from 2002 (*n* = 112) were used to document presence of *L. pertusa*. Dives were conducted following the methods described by Yoklavich et al. (2007). Four additional dives were conducted in 2010 by FED in the Channel Islands National Marine Sanctuary (CINMS) using the Kraken ROV in 2010 (Yoklavich et al., 2011). Follow up surveys by NOAA National Centers for Coastal Ocean Science (NCCOS) targeted 13 locations of known *L. pertusa* occurrences in 2014 and 2015 using Marine Applied Research and Exploration's (MARE) Beagle ROV (Caldow et al., 2015).

Coral Photo/Video Analysis

Locations of *L. pertusa* were identified by reviewing both video footage for sub dives and a large photographic database (*n* = 47,380) derived from SWFSC's combined surveys. When *L. pertusa* was identified in the photo database, those dives were marked for full video review seeking additional occurrences (*n* = 58). Video footage from 116 dives in 2002 (*n* = 112) and 2010 (*n* = 4) were reviewed for *L. pertusa* occurrence. Surveys in 2014 and 2015 (*n* = 28) targeted regions of known

L. pertusa depth and/or location. New occurrences were added if not already documented from the previous surveys. Discrete occurrences were defined as occurrences of *L. pertusa* separated by at least 3 min, or on a distinctly different substrate. Coral aggregations were categorically defined as 'reef building' when framework (live and dead coral with vertical relief) was present and aggregations were >1 m^2, as 'patchy aggregations' when there was no framework and coral patches were 50 cm^2–1 m^2, as 'sparse live patches' when coral patches were <50 cm^2, and 'rubble only' when no live coral was present.

Sampling

One collection was taken in 2010 using the Kraken ROV (M2-10-02-Lophelia, later designated as Smithsonian Sample UNSM1148068). Remaining sample collections were all taken with the MARE Beagle ROV in 2014 and 2015 under NOAA National Marine Sanctuaries permit number CINMS-2015-002. Samples were transported to the surface under ambient conditions. Upon reaching the surface, each collection was immediately subsampled for live, frozen, dry and 95% ethanol preservation.

Hydrographic Data

Conductivity, Temperature, Depth (CTD) and hydrographic upcast data between January 2007 and November 2015 were obtained from quarterly surveys conducted by the California Cooperative Oceanic Fisheries Investigation (CalCOFI, 2019). ArcGIS Desktop (10.1, ESRI) was used to calculate the nearest station to each coral occurrence and values at closest depth were used in analyses. The maximum distance between a CalCOFI station and *L. pertusa* occurrence was 35.5 km, and most were within 25 km. ROV temperature and salinity data were also available for most occurrences and used to evaluate the efficacy of using CalCOFI stations for predicting benthic conditions. CTD (Citadel CTD, Teledyne RDI) temperature data from the ROV was available for 81 of the occurrences; the ROV mean temperature of 9.03 ± 0.98°C was closely aligned with the mean temperature calculated from CalCOFI of 9.04 ± 0.41°C.

Carbonate Chemistry

Aragonite saturation states (Ω_{Arag}), dissolved inorganic carbon (DIC), pH, [$CO_3{}^{2-}$] and total alkalinity (TA) of seawater were calculated empirically using algorithms (Alin et al., 2012) and directly through water sampling using CTD-rosette in 2010 and 2015. The empirical relationships ($r^2 > 0.98$ for all but TA; TA $r^2 = 0.927$) developed by Alin et al. (2012) were specific to the southern California Current System. They use temperature (T), oxygen (O), salinity (S), and potential density (σ_Θ) to estimate various parameters of the carbonate system. Reference values ($T_r = 10.28°C$, $O_r = 127.80$ μmol kg^{-1}, $S_r = 33.83$, $\sigma_{\Theta r} = 25.97$) represent average temperature, oxygen, salinity and potential density values over the study area and were restricted to depths of *L. pertusa* occurrences. In April 2015, CTD-rosette casts were conducted directly adjacent to *L. pertusa* aggregations in CINMS (Caldow et al., 2015; Hennige et al., 2020). Total alkalinity was determined by potentiometric titration and DIC by coulometric titration. Additional carbonate parameters were calculated in CO2SYS (Lewis and Wallace, 1998). Aragonite saturation values from 2010 (D. Lipski, NOAA unpublished data) were associated with a habitat characterisation of Piggy Bank described in Yoklavich et al. (2011), Caldow et al. (2015), Hennige et al. (2020). Note the close match between Ω_{Arag} values collected from water samples (red circles) and the empirical algorithms (box plots) in **Supplementary Figure 2**.

Experimentally Incubated Samples

Live and dead *L. pertusa* specimens collected from the Mingulay Reef Complex were subjected to 12 month incubations under five different scenarios in Hennige et al. (2015a); (i) 9°C 380 ppm (the ambient environment); (ii) 9°C 750 ppm (ambient temperature, elevated CO_2); (iii) 12°C 750 ppm (elevated temperature, elevated CO_2); (iv) 12°C 380 ppm (elevated temperature and ambient CO_2); and (v) 9°C 1000 ppm (ambient temperature, elevated CO_2). At the end of the experiment, samples were dried and stored for subsequent skeletal analysis here. For each treatment, there were four replicate systems, each comprising four 5 l tanks connected to a 60 l sump (Hennige et al., 2015a,b).

Synchrotron Radiation Micro-Computed Tomography Imaging

Synchrotron radiation micro-computed tomography scans (SRμCT) were performed at the Diamond Light Source at the Harwell Science and Innovation Campus, Oxfordshire, United Kingdom (sessions MT19794 and MT20412) on the I13-2 Diamond-Manchester branchline of I13 beamline. The Insertion Device (ID) source positioned in the electron beam orbit generates X-rays ∼250 m from the sample position. The X-ray beam passed through a horizontally reflecting platinum X-ray mirror before reaching the sample. Propagation based phase contrast imaging was performed with a pink beam centred on an energy of 27 keV. This allowed the reduction of dose to the samples, i.e., using higher photon energies reduced the absorption of the X-ray by the specimen, and retrieved phase-sensitive images that reveal gradients and de-mineralisation profiles. A 500 μm CdWO$_4$ scintillator converted X-rays into visible light, and a pco Edge 5.5 camera with 1.25x Olympus objective focussed onto the scintillator was used to generate the images. This combination of optics resulted in a voxel size of $2.6 \times 2.6 \times 2.6$ μm^3. We gathered 2500 projections between 0° and 180° at an angular increment of 0.072°, an exposure time per projection of 0.05 s, and a distance between sample and camera objective of 100 mm. In total, 75 live and dead corallites from the 10 sites of ∼200 mm^3 were scanned yielding reconstructed datasets of $2160 \times 2560 \times 2560$ voxels in 32 bit. Data reconstruction was performed using Savu, a modular reconstruction pipeline with a plugin style architecture (Atwood et al., 2015; Wadeson and Basham, 2016) that makes use of the ASTRA toolbox (van Aarle et al., 2015, 2016). Custom software was developed in Python (Python Software Foundation, version 2.7.) using Numpy (Oliphant, 2007) and skimage (van der Walt et al., 2014) libraries to determine porosity ρ. To do so, images were cropped and smoothed slice-wise with a Gaussian filter with a standard deviation of 1. Subsequently, a threshold value

was determined on the middle 500 slices of the corallite, i.e., a significant portion of the scanned volume, using an automatic thresholding algorithm (Otsu, 1979). The porous coral volume (CV) was determined by counting all voxels above the threshold. Afterward, slice-wise closing was performed omitting planar porosity larger than 2500 pixels, i.e., parasitic pores or grown structural connections. Non-porous total volume (TV) was determined by counting all voxels in the closed, thresholded image, and porosity was determined as $\rho = 1 - CV/TV$ (see **Supplementary Figure 5**). Note, this represents a conservative measure, as we used whole mid-portions of corallite volumes as volumes of interest. If smaller volumes of interest are used, porosity was found to be considerably higher.

To verify findings, we sampled corals from previous laboratory mesocosms (Hennige et al., 2015a) and obtained SRμCT datasets at the same voxel size (session MT20412). We adapted our SRμCT scanning protocol based on previous experience so that exposure time per projection, and distance between camera and sample were increased to 0.07 s and 150 mm, respectively. A benefit of using a synchrotron is that image acquisition, reconstruction, and analyses are not affected by detection artefacts and no measurable effects on resulting images were detected from different shutter times. Porosity was calculated similar to the *in situ* samples but using 300 slides instead of 500 due to limited computational resources in this instance. Porosity was then correlated with aragonite saturation in Gnu R using a log-conversion of the non-linear data.

Nanoindentation

This technique was used to calculate plain strain modulus (stiffness), hardness, and a surrogate for ductility calculated as plastic mechanical work divided by total mechanical work. Stiffness relates to the ability of a material to resist elastic deformation, where it will return to its original state when an applied force is removed. Hardness is used here as a surrogate measure of yield strength (due to a lack of data) which represents the threshold where the material would start to be irreversibly deformed. We use the ratio between plastic mechanical work, i.e., dissipated energy, and total mechanical work of the indentation process as a surrogate measure for ductility (Spiesz et al., 2012; Mirzaali et al., 2016).

Sample Preparation

Forty Five samples of *L. pertusa* were analysed, 23 of which were dead and 22 were covered with living tissue. Soft-tissue was removed with a water jet and skeletal samples were prepared following previous protocols for mineralised tissues (Wolfram et al., 2010; Mirzaali et al., 2016). Samples were cut into sections for moulding using a Dremel. Sections were embedded, not infiltrated, in EpoHeat epoxy (Buehler). The resin cured under vacuum for 60 min to fill the intra-septal space. Once the resin had cured, the sample discs were extracted from the mould and cut with a precision bandsaw (Exakt) so that a longitudinal section of the coral was exposed at the surface. Samples were ground parallel using P1200 silicon carbide paper for 10 min intervals with intermediate checks. Once samples were parallel, they were polished with increasing grades of silicon carbide

paper P1200, P2000, and P4000 for 8, 10, and 15 min at 300 rpm, respectively, and polished with 0.25 μm diamond paste for 8 min. Between each step, samples were cleaned in an ultrasound bath for 7 min.

Indentation was performed using a Berkovich diamond tip mounted to a depth-sensing, force controlled nanoindenter (Hysitron). The force applied to the tip followed a monotonic ramp up to 50 mN over the course of 60 s. At that point, force was held constant for 30 s before being totally unloaded in 7.5 s (Wolfram et al., 2010; Mirzaali et al., 2016). Each sample was indented 35 times in seven groupings of five indents. Each group of five was at a different transverse location, and each indent in a group was at a different radial location. Indentations were sufficiently spaced to avoid interference between indentations and were placed at least seven-times the indentation depth away from the embedding interface, thus avoiding embedding effects (Wolfram et al., 2010). In total, 1635 indentations were carried out. Indents were grouped, as no significant difference was measured between radial and transverse locations ($p > 0.78$). Scipy's trapezoidal method (Jones et al., 2001) was used in Python (Python Software Foundation, version 2.7.) to integrate force-depth curves to calculate work. The integration was carried out for the loading and holding section to find total indentation work (W_{tot}) while elastic work (W_e) was found by integrating the unloading section. The difference between total indentation work (W_{tot}) and elastic work (W_e) gives dissipated energy, i.e., plastic work (W_{pl}). The indenter was tested on a fused quartz sample to check its calibration, the same sample used to produce the tip area function. The measured value for plain strain modulus was 69.34 GPa, where the reference value for the sample supplied was 69.6 GPa. Hardness was within 10% of the reference value. In total, 476 indentations could not be used for analysis due to failed indentations, potentially as a result of holes (submicroscopic porosity, potentially the dark areas around the pores in the inlay in **Figure 4G**) not visible when assigning the indentation position, or due to surface roughness from the preparation protocol (Fischer-Cripps, 2002). To check the latter, roughness was tested on $n = 10$ samples with an electric surface roughness tester (Taylor Hobson Talysurf 5–120) working on a carrier modulating principle. We tested five samples where failed indentations had occurred and five samples where all indentations were successfully completed. No significant difference in roughness ($p = 1$) was found, and median roughness (R_a) of the samples was 2.3 nm (2.0–3.3 nm). Surface quality was considered sufficient for indentations >500 nm as conducted in this study.

Raman Imaging and Electron Backscatter Diffraction

To assess the biomineralisation aspects we used three live and three dead samples from each of the 10 sites resulting in a total of 60 samples. Samples were embedded, not infiltrated, in EpoHeat epoxy (Buehler). Resin was cured under vacuum for 60 min and cross-sectioned using a slow saw. Samples were polished using progressive grits of silicone carbide paper (P320, P1200, P2500, P4000), micropolished using alpha aluminium oxide at

1 and 0.3 μm, and fine-polished with 0.06 μm amorphous colloidal silica (Buehler) on a short nap to remove any residual damaged surface layers (Hennige et al., 2015a). To assess the compositional properties of the skeleton, Raman spectroscopy was used (Hennige et al., 2014a, 2015a) with a Renishaw inVia Raman Spectrometer equipped with a Leica DM 2500M microscope and 785 nm laser, with the aragonite peak centred at 1085 cm^{-1}. Full Width Half Maximum (FWHM) measurements of the aragonite peak at 1085 cm^{-1} were collected at the outside tips of newly grown polyps, as close as possible to the sample edge (∼5 μm). Electron Backscatter Diffraction (EBSD) was used to investigate crystal composition. A FEI Quanta 200F field emission scanning electron microscope (SEM) equipped with a TSL EBSD system (Hennige et al., 2015a). Grain CI tolerance was 5 with a minimum grain size of 2 pixels, neighbour CI correlation was 0.05. The Kikuchi patterns were indexed using the Orientation Imaging Microscopy (OIM) Data Collection database, which contains structure files of aragonite. OIM maps were subject to two clean-up algorithm procedures to ensure reliable data were displayed, where grain CI standardisation was applied with a grain tolerance of 5, minimum grain size of 2 pixels, and neighbour CI correlation of 0.2. Further partitioning of data was applied with only grains of CI Fit and displayed in the resultant OIM map to remove background noise from the final dataset (Cusack et al., 2008).

Gravitational Density Measurement

Skeletal density was determined using a pycnometer with methanol (COH$_4$) on four dead and four live samples representing the extremes of the sample spectrum. Pycnometers are used to measure relative density (Swartz, 1962; Titschack et al., 2016) of the solid phase in granular materials excluding the confounding impact of the pore phase. Samples were ball milled (Retsch MM 200) at a frequency of 25 Hz for 40 min to attain ∼1 μm grain size. Therefore, the investigated particle volume was ∼1 μm^3 which is at least an order of magnitude smaller than the SRμCT porosity measurements which were obtained at a voxel size of 2.6 μm. Pycnometer volume was then determined measuring the dry weight of the pycnometer with a high precision lab scale (SE 203-LW, VWR). After the room temperature was determined, the pycnometer was filled with methanol and filled weight was measured m_{sf}. Density of methanol was determined in ambient conditions using the pycnometer volume of $V_s = 24.808$ cm^3 as $\rho_{meth} = \frac{(m_{sf}-m_s)}{V_s}$. Subsequently, the pycnometer was emptied, dried and a CWC sample ball milled to a grain size of ∼1 μm was inserted. Combined weight of CWC dust and pycnometer m_p was measured, and sample weight $m_e = m_p - m_s$ calculated. Methanol was added, then the pycnometer was vacuumed to remove potential air bubbles and closed. The combined weight $m_1 = m_s + m_e + m_{meth}$ was then measured. Volume of the coral material was determined as $V_e = V_s - \frac{(m_1-m_s-m_e)}{\rho_{meth}}$ so that the density of the coral material ρ_e was calculated as $\rho_e = \frac{m_e}{V_e}$. One sample was not usable due to lack of material available for the measurement. A *post hoc* power analysis (pwr package, Gnu R) (R Development Core Team, 2008) validated the number of used samples. To detect a

significant difference of 10% in the material density, which we deemed necessary to trigger significant differences in mechanical response, $n = 3.45$ specimens would have been needed. For the power analysis, we used a joint standard deviation of 0.1 g/cm^3, a power of 0.8, and a significance level of 0.05 for a two-sample test. Joint standard deviation was larger than the one encountered for the used groups. Accounting for the lost sample in the power analyses with different group sizes indicated that groups of $n_1 = 2.98$ and $n_2 = 4$ were sufficient for the analyses.

X-Ray Diffraction

X-ray diffraction samples in three groups [live, dead, and samples with both live and dead parts (hybrid)] were ground to powder in a mortar, and deposited manually as a thin layer onto a Si510 wafer in an L510 PMMA sample holder. XRD was performed using the Bruker D8 Advance diffractometer Bragg-Brentano geometry with a Lynxeye position-sensitive detector, Cu Kα radiation, and sample spinning. Parameters used include divergence slit V12, scatter screen height 5 mm, 45 kV, 40 mA, and detector settings: LL 0.11, W 0.14. Measurements were performed via a coupled scan 10°–110° with step size 0.020° and a counting time per step of 2 s. The diffractograms were analysed using the Bruker software DiffracSuite.EVA v4.2. Crystalline structures were assigned through comparison of experimentally determined peak positions and intensities with the ICDD pdf4 database. Thereafter, results were refined using the Profex/BGMN Rietveld refinement software, for which complete XRD patterns were used. Five specimens per group were tested.

Constitutive Modelling for Illustrating the Effect of Porosity

We illustrate the effect of increasing porosity with a 1D linear elastic-plastic material model. A previously implemented model was used (Mirzaali et al., 2015), without damage and asymmetric yield stresses but with an ideal plasticity (Lemaitre and Chaboche, 2000). Stiffness of the coral material was obtained from the nanoindentation experiments and subjected to increasing amounts of porosity, so that E = $(1 - CV/TV)$E*, with CV/TV the volume fraction of a region of interest in the skeletal wall. Yield stress or strength have not yet been reported for coral material on micron-sized volumes. Yield stress here was estimated based on a comparison with the extracellular matrix in bone, another mineralised tissue. Since hardness is a yield surrogate, the ratio between strength in bone tissue (Mirzaali et al., 2015) and hardness determined by microindentation were used to estimate the yield stress, so that $\sigma_y = (1 - CV/TV)\sigma_y^{est}$. Although it is clear that micromechanical strength experiments such as those determined by Schwiedrzik et al. (2014) and Groetsch et al. (2019) need to be performed to fully understand the non-linear mechanical behaviour of CWC, the estimation of the micromechanical yield stress done here is sufficient to illustrate the effect of increasing porosity on load bearing capacity. Furthermore, we assume that stiffness and strength are affected in the same way by porosity so that the yield strain is the

same for increasing porosities. This is not necessarily the case as has been shown for bone tissue (Wolfram et al., 2012).

Statistical Analysis

Descriptive statistics and statistical testing were performed using Gnu R (R06) (R Development Core Team, 2008). A significance level of $p = 0.01$ was chosen before comparisons were made. Normality was checked using Shapiro-Wilk normality tests and rejected ($p < 10^{-5}$). This was verified by Q-Q plots of the quantiles of the collected data vs. the quantiles of the normal distribution which showed non-linear curves. Therefore, median and range were chosen for descriptive statistics and non-parametric Wilcoxon rank-sum tests were used in groupwise comparisons (Crawley, 2005). R's linear regression model was used to investigate regressions between continuous variables, e.g., plain strain modulus and aragonite concentration. *Post hoc* power analyses were performed using R's pwr library and methods (see section "Gravitational Density Measurement").

RESULTS

In situ Evidence: The Southern California Bight

Lophelia pertusa occurrences were documented across the Southern California Bight in visual fisheries surveys conducted using remotely operated vehicles (ROV) from 2002 to 2012 (Salgado et al., 2018) and in targeted, follow-on visual surveys in 2015 (Caldow et al., 2015). *L. pertusa* was found on most banks, seamounts and ridges surrounding the Channel Islands (**Supplementary Figure 1**, with corresponding location data in **Supplementary Table 1**). Though widely distributed, with numerous occurrences ($n = 132$) at 313–66 m depth, the majority of sites had only sparse live or dead patches ($<1 m^2$). Occurrences of reef building coral assemblages (with live and dead skeleton framework) increased nearly 4-fold (from 5 to 18%) from below to above the ASH ($n = 181$ data points, **Supplementary Table 1**). The highest frequency and abundance of coral was found in the Channel Islands National Marine Sanctuary (CINMS) on the peak of the Piggy Bank Seamount and along the ridge of the Footprint feature (**Supplementary Figure 1**). Studies in 2014 and 2015 targeted these sites for water sampling and included the biological samples analysed in this manuscript. Temperatures in these regions closely match those reported globally for *L. pertusa* ($9.12 \pm 0.95°C$ *SD*), but oxygen concentrations are relatively low (2.1 ± 1 ml/l; range 0.65–5.3 ml/l).

Aragonite saturation (Ω_{Arag}) values from 2007 to 2015 near Southern California Bight *L. pertusa* sites were between 0.72 and 1.86, the lowest Ω_{Arag} conditions recorded for *L. pertusa* to date (**Supplementary Table 1**). *L. pertusa* sites that had substantial cohesive reef framework consisting of live and dead coral (**Figure 1a**) were limited to shallow sites (169–65 m, $n = 14$ sites). At depths of 169 meters mean Ω_{Arag} was 0.9 ± 0.09 with a range of 0.79–1.04. At 65 meters mean Ω_{Arag} was 1.3 ± 0.25 with a range of 0.92–2.05. Based on long-term repeat estimates of carbonate chemistry (see section "Materials and Methods"), sites below 170 m are likely to experience persistent aragonite

undersaturation ($\Omega_{Arag} < 1$ in $> 90\%$ of estimated Ω_{Arag} from 2007 to 2015; **Supplementary Figure 2**), corresponding closely to the depth below which dead reef framework was absent. The Piggy Bank site (293 m; $\Omega_{Arag} = 0.73$) had high abundance of live *L. pertusa* blanketing the seafloor but lacked structural complexity due to absence of dead framework (**Figure 1b**). The decrease in habitat complexity observed with decreasing Ω_{Arag} (**Figure 1b**) strongly indicates that the foundation framework of the reef is dissolving or structurally failing under low Ω_{Arag} conditions once soft-tissue has retracted. Thus, the foundation framework is unable to support larger reef frameworks. To quantify how decreasing Ω_{Arag} affected the structural integrity of corals, samples from the CINMS within the Southern California Bight were collected for structural analysis from reef (macro) to crystal (micro) length scales (**Supplementary Figure 3**).

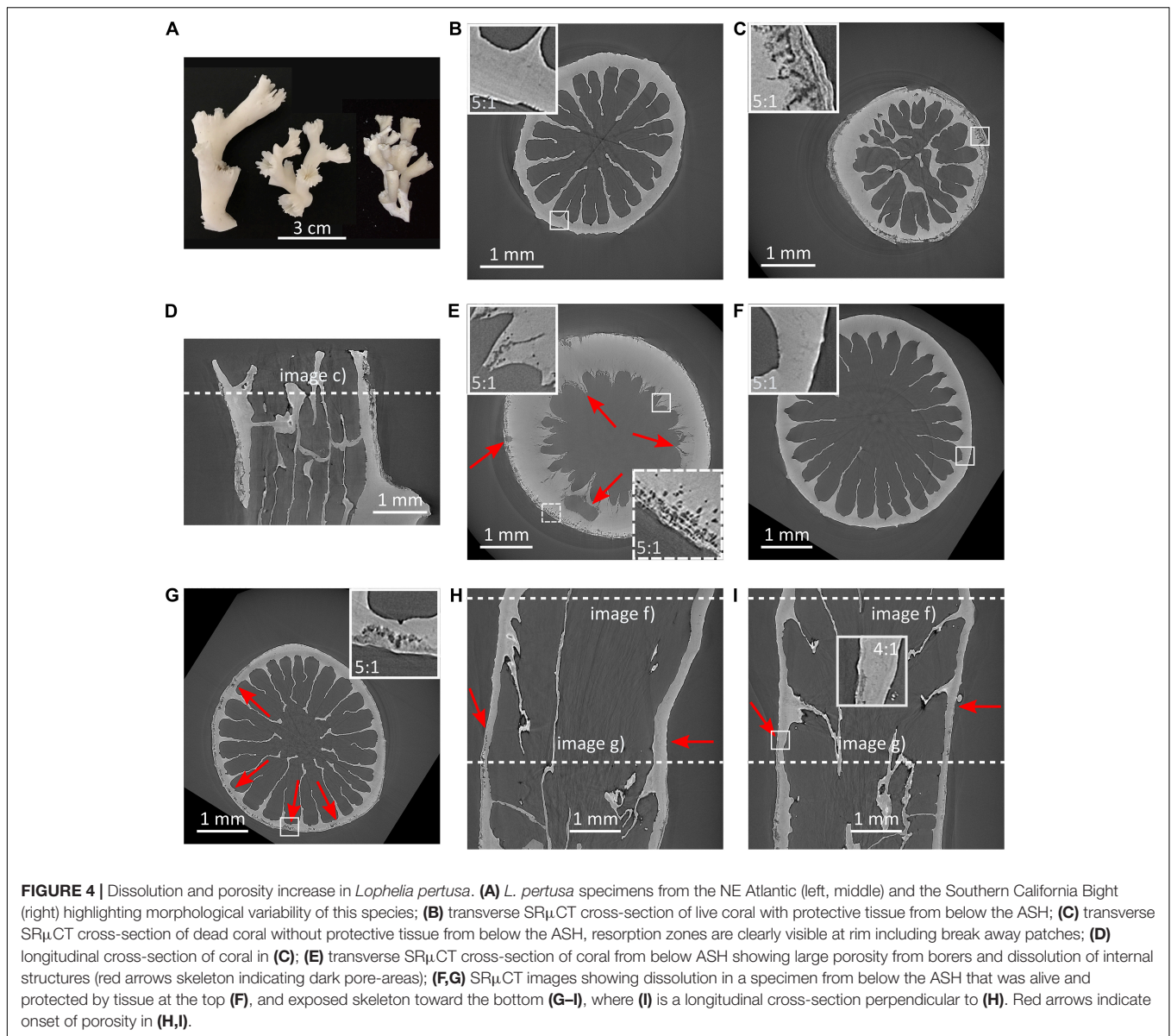### Structural and Compositional Analysis of *in situ* Corals

L. pertusa branches from above and below the ASH within CINMS were characterised by profuse budding with thin, fragile calices and little-to-no branching. The structural and mechanical properties of these corals were assessed by evaluating porosity, chemical composition, stiffness, hardness, ductility and density from crystal-to-reef scales. Results are presented as images (**Figures 4**, **5**) and graphically (**Supplementary Figure 4**).

Porosity

Porosity of the *L. pertusa* skeletal material was analysed with synchrotron radiation micro-computed tomography (SRμCT). The SRμCT images highlighted increased skeletal porosity in dead coral skeleton (dark pore-areas appearing in the coral skeleton) exposed to aragonite undersaturated water [**Figure 4A** and **Supplementary Video 1** (from corals below ASH) and **Supplementary Video 2** (from experimentally incubated corals)]. Live coral exhibited no skeletal porosity, regardless of whether it was above or below the ASH when sampled (**Figure 4**). Dead samples from below the ASH exhibited increased skeletal porosity on both the outer walls and inner walls (**Figures 4C–E**). In cases where skeletons included both soft-tissue covered and non-covered portions, porosity was visible only in the exposed sections of skeleton (**Figures 4F–I**). Porosity (**Figure 5** and **Supplementary Figure 5**) increased in dead framework once the protective soft-tissue layer had retracted (**Supplementary Figure 6**). Skeletal mass density did not statistically differ between live and dead samples (**Supplementary Figure 7**).

Porosity and Material Structural Properties (Stiffness, Hardness, and Ductility)

To understand coral skeletal behaviour over time scales, it is critical to understand both the presence/absence (**Figure 5A**) and structural properties (**Figure 5B** and **Supplementary Figure 4**) of the "building blocks" of coral skeletal material under different environmental conditions. Results below indicate that while material is lost (increasing porosity), the structural properties of the material on the microscale do not change. This means that the loss of structural integrity for whole coral samples is

FIGURE 4 | Dissolution and porosity increase in *Lophelia pertusa*. **(A)** *L. pertusa* specimens from the NE Atlantic (left, middle) and the Southern California Bight (right) highlighting morphological variability of this species; **(B)** transverse SRμCT cross-section of live coral with protective tissue from below the ASH; **(C)** transverse SRμCT cross-section of dead coral without protective tissue from below the ASH, resorption zones are clearly visible at rim including break away patches; **(D)** longitudinal cross-section of coral in **(C)**; **(E)** transverse SRμCT cross-section of coral from below ASH showing large porosity from borers and dissolution of internal structures (red arrows skeleton indicating dark pore-areas); **(F,G)** SRμCT images showing dissolution in a specimen from below the ASH that was alive and protected by tissue at the top **(F)**, and exposed skeleton toward the bottom **(G–I)**, where **(I)** is a longitudinal cross-section perpendicular to **(H)**. Red arrows indicate onset of porosity in **(H,I)**.

driven by loss of material rather than a change in the underlying material behaviour.

Porosity is significantly higher in dead samples compared to live samples from below the ASH (**Figure 5A**, $p < 10^{-5}$). Instances of porosity in live samples (e.g., orange dots > 1 at an aragonite saturation of 0.7 in **Figure 5A**) are driven by small patches of tissue retraction and exposed skeleton in some samples (**Figures 4H,I**). Stiffness, hardness, and ductility are three mechanical characteristics of a material measured at micrometre length scales through nanoindentation (Fischer-Cripps, 2002; Mirzaali et al., 2016), where a diamond tip is pressed into the material with a known force (see "Materials and Methods"). Hardness and ductility allow evaluation of the material's ability to resist plastic deformation and, ultimately, failure. Skeletal material in live and dead samples across sites (above and below ASH) did not statistically differ with regard

to stiffness or hardness (**Figure 5B**, $p = 0.081$ and $p = 0.729$, **Supplementary Figure 4B**) but median ductility was 2.5% higher in the dead samples ($p < 10^{-5}$) than in the live samples (**Supplementary Figure 4D**).

While the above effects are demonstrated and modelled on individual branches of coral, the models and units used are scalable (**Supplementary Figure 8**). Units can be modified in multiple dimensions (e.g., length, width, wall thickness) and joined together through computational and mathematical modelling to construct a framework for habitat-scale interrogation.

Mineral Composition

Mineral composition was also assessed across environmental gradients, to assess whether the *type* of calcium carbonate varied. *L. pertusa* coral skeletons across sites and in live and

FIGURE 5 | Porosity and mechanics of CINMS *Lophelia pertusa*. The Figure shows **(A)** porosity of the skeletal volume, and **(B)** stiffness (plain strain modulus) of the skeletal material. Data represented as medians with min/max error bars for both axes at respective median (large diamond). Significant differences between live and dead samples are indicated by *. See also **Supplementary Figure 4** for Raman crystallinity, electron back scatter diffractions and other material chemistry of samples. Solid lines indicate ranges (min-max) around the median (large diamond) for ordinate and abscissa for live and dead samples, respectively.

dead samples were primarily composed of aragonitic crystals (**Supplementary Figure 6C**), but crystals were smaller in live corals exposed to aragonite undersaturated conditions than those in live corals exposed to oversaturated conditions. This is indicated by more black areas in **Supplementary Figures 4, 9**, where post-processing to determine alignment of crystals could not distinguish between data noise and individual crystals (crystal size below detection minimum). In live corals, we observed samples containing pure polymorphs of aragonite (X-Ray diffraction, see "Materials and Methods"). In the recently dead coral skeletons tested, we found mean weight percentages of 99% aragonite and 1% calcite. Compositional analysis by Raman spectroscopy did not reveal any differences between live and dead samples from different aragonite saturation conditions (**Supplementary Figure 4**). The absence of a difference in the compositional properties between live and dead samples indicates that the variation observed in the micromechanical properties is due to testing differently oriented crystal arrangements ("sclerodermites," **Supplementary Figure 3**). This held true for all samples above or below the ASH and along our Ω_{Arag} range, ruling out a systematic difference in the mechanical properties of the building material. Furthermore, this lack of difference in the micromechanical properties indicates that similar skeletal properties can be achieved with varying crystal sizes, indicating that the mineralisation process is very robust.

Evidence From Controlled Laboratory Experiments

To provide greater context to analysis of *in situ* samples and to understand the weakening mechanisms and timeline, we reanalysed existing live and dead *L. pertusa* samples from previous experiments (Hennige et al., 2015a), where corals from the Mingulay Reef Complex (North Atlantic) were collected and different subsamples were subjected to projected changes in

temperature and Ω_{Arag} for 12 months, ranging from $\Omega_{Arag} = 1.46$ to $\Omega_{Arag} = 0.76$. At the start of the experiment, all live corals had complete soft-tissue coverage, but following 12 months of experimentation, some fragments experienced soft-tissue retraction leaving parts of their skeleton exposed to seawater (**Supplementary Figure 10**). Coral that was alive did not exhibit an increase in porosity with increasing acidity (decreasing Ω_{Arag}) over 12 months, with the exception of small patches under elevated CO_2 conditions where soft-tissue retraction was evident (**Figure 6**). Coral that was collected alive with subsequent soft-tissue removal prior to placement in experimental treatments (classified here as dead skeleton) exhibited clear increases in porosity over the whole exposed skeleton as Ω_{Arag} decreased (**Figure 6**). This matches our observations from *in situ* samples in **Figure 4** and provides a timescale that these impacts can be observed in as little as 12 months once a critical aragonite saturation has been reached. Porosity values of 28% (27.9 ± 7.9%) were determined from $n = 10$, $(130 \, \mu m)^3$ volumes of interest in dead coral walls following exposure to the lowest aragonite saturation conditions (0.76 ± 0.1) for 12 months (Hennige et al., 2015a).

DISCUSSION

Habitat Loss

Here we demonstrate that *Lophelia pertusa* reefs living in aragonite undersaturated conditions analogous to those projected for most reefs by 2100 exhibit far less habitat complexity than *L. pertusa* reefs living above the saturation horizon. This is driven by loss of dead coral material that usually forms part of the visible habitat structure (**Figure 1**). Through experimental evidence, we go beyond identification of dissolution, and demonstrate the rapid onset of the process (quantified from 12 month experiments) in the "building blocks" of coral framework (individual coral branches), and the

FIGURE 6 | Porosity in experimentally incubated *Lophelia pertusa*. **(A)** SRμCT cross-section images of corals from Mingulay Reef Complex (Hennige et al., 2015a) subjected to different treatments of increased levels of CO_2 during 12 month laboratory incubations. **(B)** corresponding porosity analyses shows a significant, non-linear relation between porosity [red arrows in **(A)**] and aragonite saturation in dead samples ($p = 0.0008$, $r^2 = 0.59$) but no significant relationship ($p = 0.67$) for live samples. Relationship is illustrated by multi-linear curve connecting the medians.

mechanism that could lead to potentially rapid ecosystem-scale habitat loss in the near future (**Figures 3–5**). Porosity in the dead skeleton leads to a weakening of the coral (also noted in tropical examples; Scott and Risk, 1988). On the scale of a colony, which both baffles mobile sediments and supports the larger, complex reef structure, loss of structural integrity could contribute a crumbling of the larger habitat resulting in smaller aggregations of live coral with less 3-dimensional complexity and massively reduced reef/mound-building potential (**Figure 2** and **Supplementary Table 1**, *in situ* Results). Importantly, it is the *location* of the porosity in addition to the extent that underlies this process, meaning that even relatively small changes can lead to significant structural weakening. While breaking of coral under its own weight and normal bio-erosion are established (but sporadic) ways in which CWC patch reefs can expand under normal conditions (Wilson, 1979), the systemic weakening and ultimate loss of the foundation framework from ocean acidification would prevent future reef and mound growth, and lead to an ecosystem-scale habitat loss for existing coral reefs. Existing mound structure, where carbonates are buried within sediment, would not be subject to such crumbling effects.

This ecosystem-scale habitat loss, leading to a shift from one habitat type (high complexity with high biodiversity support) to another (low complexity with low biodiversity support), is generally very different from the processes described in tropical corals, where the main threat is a change in growth rates of live coral combined with greater bioerosion efficacy. While increased acidity and enhanced bioerosion activities can also lead to decreased structural integrity and density in tropical corals (Scott and Risk, 1988; Enochs et al., 2014), the risk to the overall habitat on the ecosystem scale is arguably the long-term reduction in net coral reef growth, as opposed to structural failure-induced loss of the critical (and visibly often the largest component) dead part of CWC reefs. A key part of this is the aragonite undersaturation that CWC reefs will be subjected to, and the vastly slower growth rates of the branching CWC *L. pertusa* compared to branching tropical analogs. While bioerosion is a key process on reefs through prograding and propagation of corals in both tropical and deep-sea corals (Wilson, 1979; Tunnicliffe, 1981), it is unclear how well CWC would fare if living coral "fell" (following loss of habitat integrity) into habitat areas with water flow inadequate for heterotrophic feeding

(Purser et al., 2010), as unlike tropical coral, they cannot acquire photosynthetic carbon.

Mechanical and Mineral Properties of CWC Skeletons

With regard to skeletal stiffness and hardness, our data were comparable to those recorded in shallow-water zooxanthellate corals around localised volcanic acidification sites with low pH conditions (Fantazzini et al., 2015; Pasquini et al., 2015), where Fantazzini et al. (2015) reported an ∼8% difference in stiffness but no difference in hardness over 0.4 pH points. While similar, results are not directly comparable to CWC investigated here due to the higher aragonite saturation ($\Omega_{Arag} > 1$) of the volcanic sites used, and the zooxanthellate nature of the shallow corals. Here, *L. pertusa* skeletal material properties measured at the micrometre length scale changed very little across aragonite saturation for live or dead samples, but exposed, dead coral skeleton showed significantly increased porosity driven by dissolution in aragonite undersaturated conditions (**Figure 5**). This is contrasted by no significant difference in skeletal mass density between live and dead samples from above and below the ASH. Other studies (e.g., Mollica et al., 2018) have measured a decrease in coral skeletal density due to ocean acidification, and the contrast to results here can be explained by length scale. When using a clinical type CT scanner, typical resolution is orders of magnitude larger than the porosity observed here. Porosity assessed using clinical type CT scanners would be visible through a lower X-ray attenuation, which translates into a lower density. The combined effect of constant skeletal mass density on a micrometre length scale with increased skeletal porosity, as identified here, explains lowered *macroscopic*, skeletal mass density. This further underlines the important finding that the mineralised skeleton produced below the ASH is of similar quality compared to that above the ASH. The processes observed here in CWC occurred in both thin and thick coral branches. For instance, Mingulay corals had thicker morphotypes than those sampled from the Pacific (**Figure 4**; Form and Riebesell, 2012; Hennige et al., 2014b, 2015a; Büscher et al., 2017).

In instances where calcite (1%) was observed in recently dead coral skeletons, it is possible that calcite incorporation is linked to aragonite precipitation (Farfan et al., 2018). While changes in Electron Backscatter Diffraction (EBSD) results here were driven by changes in crystal size rather than type, recent work (Farfan et al., 2018) has also shown that in some cases the incorporation of calcite in *L. pertusa* can be up to 3%, with highest values found in dead samples from deep sites. The decrease in crystal size in corals from below the ASH is consistent with observations (Hennige et al., 2015a), where *L. pertusa* samples were incubated in mesocosms of projected future conditions.

Challenges and Opportunities

While we demonstrate here that accumulation of significant porosity is rapid (12 month laboratory incubations), and that the likely impacts of this can be seen at a large scale through *in situ* evidence, there are a number of factors to integrate into future work to be able to determine *when* CWC habitats will undergo ecosystem scale changes with regard to their complexity. Timescales are key, and while significant porosity is observed within 12 months, to model when that will have reef-scale impacts we need to quantify the linear/non-linear progression of porosity under different scenarios. Scaling up from our conceptual models to reef-scale habitats will be achieved through computational and mathematical techniques, which can build directly upon findings we have conceptualised here (e.g., **Supplementary Figure 8**). Timescales of coral degradation in large habitat structures are also important to consider, as over a long period of time, dead coral framework will be biofouled and infilled with sediment. As *in situ* evidence demonstrates, once in aragonite undersaturated water, CWC habitats have reduced complexity. Given this, it seems plausible that loss of dead coral material outpaces amelioration by sediment infilling or biofouling, but the rate of growth:loss (and carbonate budgets as a whole) are a critical challenge for the field to address. An important contributor to this process is bioerosion (Wisshak et al., 2012; Büscher et al., 2019), which will contribute significantly to a weakening of the coral structure (Tunnicliffe, 1979). While no bioerosion was observed in experimentally incubated samples here, bioerosion was evident in some samples collected *in situ* (e.g., **Figure 4E**). Including the *rate* of bioerosion contribution will be important for future models as it will contribute significantly to the rate of structural weakening and crumbling of reefs overall.

Underlying these processes is the need for greater understanding of the rates of seawater carbonate chemistry changes. The progression and timescale of increased porosity *in situ* will depend on whether the aragonite undersaturation of the water is consistent (does it fluctuate above or below $\Omega_{Arag} = 1$), biological respiration enhancing localised acidification, dissolution of carbonates (Sarma et al., 2002), the coverage of exposed skeletal material by sediment or manganese oxide, and the extent of change of other key environmental variables such as temperature (a key determinant of carbonate chemistry) and deoxygenation (which may contribute to increased skeletal exposure through death or tissue retraction of the live coral). Given the lack of dead skeletal framework in **Figure 1b**, it seems likely that the timescales of material loss and habitat crumbling are faster than any mitigating processes, but to determine risk of habitat loss, repeated measure studies on live and dead coral, and refined models are needed.

CONCLUSION

The techniques used in this investigation to measure and model "porosis" in CWC build upon those routinely used to examine bone porosis (osteoporosis). The parallels that can be drawn as a result of this are of benefit to modelling "porosis" in CWC, as the independent variables investigated in this study, such as aragonite saturation, seem to offer a potential predicting metric if quantified locally over sufficient time scales. This would allow adaptation of diagnostic principals (Currey, 2002; Kanis et al., 2008; Hernlund et al., 2013; Engelke et al., 2016; Mirzaali et al., 2016; International Osteoporosis Foundation [IOF], 2019; Lefèvre et al., 2019) to model "coralporosis" and to identify tipping

points of CWC habitat loss (Dakos et al., 2019). While we describe the potentially rapid detrimental effects of ocean acidification to CWC reefs of the future along with the underlying mechanisms, it is this ability to model such changes that may give us powerful monitoring tools for deep-sea reefs. As we develop models supported by refined projections of changes in aragonite saturation, timescales of change and quantification of the proportion of CWC habitat comprised of dead (at risk) material, this will ultimately support future conservation and management efforts of these vulnerable marine ecosystems by indicating *which* ecosystems are at risk, *when* they will be at risk, and *how* much of an impact this will have upon associated biodiversity.

DATA AVAILABILITY STATEMENT

Data supporting the conclusions of this article are available through the authors and through the British Oceanographic Data Centre (Hennige et al., 2020).

AUTHOR CONTRIBUTIONS

SH, UW, LW, JMR, FM, and PE designed the concept of this manuscript. SH, LW, NK, UW, ES, AG, SS, and M-EA-T conducted the experimental analysis. All authors were involved in discussion. PE solicited funding for the fieldwork and led the *in situ* sampling effort, with assistance from LW.

FUNDING

ACKNOWLEDGMENTS

SUPPLEMENTARY MATERIAL

The Supplementary Material for this article can be found online at: https://www.frontiersin.org/articles/10.3389/fmars.2020.00668/full#supplementary-material

REFERENCES

Albright, R., Takeshita, Y., Koweek, D. A., Ninokawa, A., Wolfe, K., Rivlin, T., et al. (2018). Carbon dioxide addition to coral reef waters suppresses net community calcification. *Nature* 555, 516–519. doi: 10.1038/nature 25968

Alin, S. R., Feely, R. A., Dickson, A. G., Martín Hernández-Ayón, J., Juranek, L. W., Ohman, M. D., et al. (2012). Robust empirical relationships for estimating the carbonate system in the southern California Current System and application to CalCOFI hydrographic cruise data (2005-2011). *J. Geophys. Res. Ocean.* 117:C05033. doi: 10.1029/2011JC007511

Atwood, R. C., Bodey, A. J., Price, S. W. T., Basham, M., and Drakopoulos, M. (2015). A high-throughput system for high-quality tomographic reconstruction

of large datasets at diamond light source. *Philos. Trans. R. Soc. A Math. Phys. Eng. Sci.* 13:373. doi: 10.1098/rsta.2014.0398

Baco, A. R., Morgan, N., Roark, E. B., Silva, M., Shamberger, K. E. F., and Miller, K. (2017). Defying dissolution: discovery of deep-sea scleractinian coral reefs in the North Pacific. *Sci. Rep.* 7:5436. doi: 10.1038/s41598-017-05492-w

Büscher, J. V., Form, A. U., and Riebesell, U. (2017). Interactive effects of ocean acidification and warming on growth, fitness and survival of the cold-water coral Lophelia pertusa under different food availabilities. *Front. Mar. Sci.* 4:101. doi: 10.3389/fmars.2017.00101

Büscher, J. V., Wisshak, M., Form, A. U., Titschack, J., Nachtigall, K., and Riebesell, U. (2019). In situ growth and bioerosion rates of Lophelia pertusa in a Norwegian fjord and open shelf cold-water coral habitat. *PeerJ* 7:e7586. doi: 10.7717/peerj.7586

CalCOFI (2019). *California Cooperative Oceanic Fisheries Investigations*. Available online at: http://www.calcofi.org/ (accessed January 24, 2019).

Caldow, C., Etnoyer, P. J., and Kracker, L. (2015). *Cruise report for 'Patterns in deep-sea corals' expedition: NOAA ship Bell M. Shimada SH*-15-03. Silver Spring, MD: NOAA Tech. Memorandum NOS NCCOS 200, doi: 10.25923/krv2-ps85

Crawley, M. J. (2005). *Statistics-An Introduction Using R*. Hoboken, NJ: John Wiley and Sons, Ltd.

Currey, J. D. (2002). *Bones: Structure and Mechanics*. Princeton: Princeton University Press.

Cusack, M., England, J., Dalbeck, P., Tudhope, A. W., Fallick, A. E., and Allison, N. (2008). Electron backscatter diffraction (EBSD) as a tool for detection of coral diagenesis. *Coral Reefs* 27, 905–911. doi: 10.1007/s00338-008-0414-3

Dakos, V., Matthews, B., Hendry, A. P., Levine, J., Loeuille, N., Norberg, J., et al. (2019). Ecosystem tipping points in an evolving world. *Nat. Ecol. Evol.* 3, 355–363. doi: 10.1038/s41559-019-0797-792

Davidson, T. M., Altieri, A. H., Ruiz, G. M., and Torchin, M. E. (2018). Bioerosion in a changing world: a conceptual framework. *Ecol. Lett.* 21, 422–438. doi: 10.1111/ele.12899

Engelke, K., van Rietbergen, B., and Zysset, P. (2016). FEA to measure bone strength: A review. *Clin. Rev. Bone. Min. Metab.* 14, 26–37. doi: 10.1007/s12018-015-9201-1

Enochs, I. C., Manzello, D. P., Carlton, R., Schopmeyer, S., van Hooidonk, R., and Lirman, D. (2014). Effects of light and elevated pCO2 on the growth and photochemical efficiency of Acropora cervicornis. *Coral Reefs* 33, 477–485. doi: 10.1007/s00338-014-1132-1137

Eyre, B. D., Cyronak, T., Drupp, P., De Carlo, E. H., Sachs, J. P., and Andersson, A. J. (2018). Coral reefs will transition to net dissolving before end of century. *Science* 359, 908–911. doi: 10.1126/science.aao1118

Fantazzini, P., Mengoli, S., Pasquini, L., Bortolotti, V., Brizi, L., Mariani, M., et al. (2015). Gains and losses of coral skeletal porosity changes with ocean acidification acclimation. *Nat. Comm.* 6:7785. doi: 10.1038/ncomms8785

Farfan, G. A., Cordes, E. E., Waller, R. G., DeCarlo, T. M., and Hansel, C. M. (2018). Mineralogy of deep-sea coral aragonites as a function of aragonite saturation state. *Front. Mar. Sci.* 5:473. doi: 10.3389/fmars.2018.00473

Feely, R. A., Sabine, C. L., Hernandez-Ayon, J. M., Ianson, D., and Hales, B. (2008). Evidence for upwelling of corrosive "acidified" water onto the continental shelf. *Science* 320, 1490–1492. doi: 10.1126/science.1155676

Feely, R. A., Sabine, C. L., Lee, K., Berelson, W., Kleypas, J., Fabry, V. J., et al. (2004). Impact of anthropogenic CO2 on the CaCO3 system in the oceans. *Science* 305, 362–366. doi: 10.1126/science.1097329

Fischer-Cripps, A. C. (2002). *Nanoindentation*. New York, NY: Springer-Verlag.

Form, A. U., and Riebesell, U. (2012). Acclimation to ocean acidification during long-term CO2 exposure in the cold-water coral Lophelia pertusa. *Glob. Chang. Biol.* 18, 843–853. doi: 10.1111/j.1365-2486.2011.02583.x

Freiwald, A., Rogers, A., and Hall-Spencer, J. (2005). *Global Distribution of Cold-Water Corals (version 2)*. Available online at: https://www.data.unep-wcmc.org/datasets/1 (accessed March, 2020).

Gammon, M. J., Tracey, D. M., Marriott, P. M., Cummings, V. J., and Davy, S. K. (2018). The physiological response of the deep-sea coral Solenosmilia variabilis to ocean acidification. *PeerJ* 6:e5236. doi: 10.7717/peerj.5236

Gómez, C. E., Wickes, L., Deegan, D., Etnoyer, P. J., and Cordes, E. E. (2018). Growth and feeding of deep-sea coral Lophelia pertusa from the California margin under simulated ocean acidification conditions. *PeerJ* 6:e5671. doi: 10.7717/peerj.5671

Groetsch, A., Gourrier, A., Schwiedrzik, J., Sztucki, M., Beck, R. J., Shephard, J. D., et al. (2019). Compressive behaviour of uniaxially aligned individual mineralised collagen fibres at the micro- and nanoscale. *Acta Biomater.* 89, 313–329. doi: 10.1016/J.ACTBIO.2019.02.053

Gruber, N., Hauri, C., Lachkar, Z., Loher, D., Frölicher, T. L., and Plattner, G. K. (2012). Rapid progression of ocean acidification in the California Current System. *Science* 337, 220–223. doi: 10.1126/science.1216773

Guinotte, J. M., Orr, J. C., Cairns, S., Freiwald, A., Morgan, L., and George, R. Y. (2006). Will human-induced changes in seawater chemistry alter the distribution of deep-sea scleractinian corals? *Front. Ecol. Environ.* 4:141–146. doi: 10.1890/1540-9295(2006)004[0141:whcisc]2.0.co;2

Hardin, D. D., Toal, J., Parr, T., Wilde, P., and Dorsey, K. (1994). Spatial variation in hard-bottom epifauna in the Santa Maria basin, California: the importance of physical factors. *Mar. Environ. Res.* 37, 65–193. doi: 10.1016/0141-1136(94)90022-90021

Hauri, C., Gruber, N., Vogt, M., Doney, S. C., Feely, R. A., Lachkar, Z., et al. (2013). Spatiotemporal variability and long-term trends of ocean acidification in the California Current System. *Biogeosciences* 10, 193–216. doi: 10.5194/bg-10-193-2013

Hennige, S., Wolfram, U., Wickes, L., Murray, F., Roberts, J. M., Kamenos, N., et al. (2020). Physical and visual effects of ocean acidification on cold-water coral (*Lophelia pertusa*) skeleton samples from the Southern California Bight, USA (2010–2015) and the Mingulay Reef Complex, UK (2012). United Kingdom: British Oceanographic Data Centre, National Oceanography Centre, NERC. doi: 10/d5g9

Hennige, S. J., Morrison, C. L., Form, A. U., Büscher, J., Kamenos, N. A., and Roberts, J. M. (2014a). Self-recognition in corals facilitates deep-sea habitat engineering. *Sci. Rep.* 4:6782. doi: 10.1038/srep06782

Hennige, S. J., Wicks, L. C., Kamenos, N. A., Bakker, D. C. E., Findlay, H. S., Dumousseaud, C., et al. (2014b). Short term metabolic and growth responses of the cold-water coral Lophelia pertusa to ocean acidification. *Deep Sea Res. II* 99, 27–35. doi: 10.1016/j.dsr2.2013.07.005

Hennige, S. J., Wicks, L. C., Kamenos, N. A., Perna, G., Findlay, H. S., and Roberts, J. M. (2015a). Hidden impacts of ocean acidification to live and dead coral framework. *Proc. R. Soc. B* 282:20150990. doi: 10.1098/rspb.2015.0990

Hennige, S. J., Wicks, L., Kamenos, N. A., Perna, G., Findlay, H. S., and Roberts, J. M. (2015b). *Physiological, Biomineralisation and Structural Measurements of the Cold-Water Coral (CWC) Lophelia pertusa in response to increases in CO2 and temperature*. United Kingdom: British Oceanographic Data Centre. doi: 10.5285/13d58735-4252-109d-e053-6c86abc0bae4

Henry, L., Navas, J. M., Hennige, S., Wicks, L. C., and Roberts, J. M. (2013). Shark spawning grounds on cold-water coral reefs: a compelling case for protection of vulnerable marine ecosystems. *Biol. Conserv.* 161, 67–70.

Henry, L. A., and Roberts, J. M. (2007). Biodiversity and ecological composition of macrobenthos on cold-water coral mounds and adjacent off-mound habitat in the bathyal Porcupine Seabight. *NE Atlantic. Deep. Res. Part I Oceanogr. Res. Pap.* 54, 654–672. doi: 10.1016/j.dsr.2007.01.005

Henry, L.-A., and Roberts, J. M. (2015). "Global biodiversity in cold-water coral reef ecosystems," in *Marine Animal Forests: The Ecology of Benthic Biodiversity Hotspots*, eds S. Rossi, L. Bramanti, A. Gori, and C. del Valle (Berlin: Springer International Publishing), 1–21. doi: 10.1007/978-3-319-17001-5_6-1

Hernlund, E., Svedbom, A., Ivergård, M., Compston, J., Cooper, C., Stenmark, J., et al. (2013). Osteoporosis in the European Union: Medical management, epidemiology and economic burden: A report prepared in collaboration with the International Osteoporosis Foundation (IOF) and the European Federation of Pharmaceutical Industry Associations (EFPIA). *Arch. Osteoporos* 8:136. doi: 10.1007/s11657-013-0136-131

International Osteoporosis Foundation [IOF] (2019). Available online at: http://www.iofbonehealth.org/facts-statistics (accessed February 14, 2019).

Jones, E., Oliphant, E., Peterson, P., and Al, E. (2001). *SciPy: Open Source Scientific Tools for Python 2001*. Delhi: Community Library Project.

Kanis, J. A., McCloskey, E. V., Johannsson, H., Oden, A., Melton, J. L. III, and Kalthaev, N. (2008). A reference standard for the description of osteoporosis. *Bone* 42, 375–467.

Kazanidis, G., Henry, L.-A., Roberts, J. M., and Witte, U. F. M. (2015). Biodiversity of Spongosorites coralliophaga (Stephens, 1915) on coral rubble at two contrasting cold-water coral reef settings. *Coral Reefs* 35, 1–16. doi: 10.1007/s00338-015-1355-1352

Kline, D. I., Teneva, L., Okamoto, D. K., Schneider, K., Caldeira, K., Miard, T., et al. (2019). Living coral tissue slows skeletal dissolution related to

ocean acidification. *Nat. Ecol. Evol.* 3, 1438–1444. doi: 10.1038/s41559-019-0988-x

Lefèvre, E., Farlay, D., Bala, Y., Subtil, F., Wolfram, U., Rizzo, S., et al. (2019). Compositional and mechanical properties of growing cortical bone tissue: a study of the human fibula. *Sci. Rep.* 9:17629. doi: 10.1038/s41598-019-54016-54011

Lemaitre, J., and Chaboche, J.-L. (2000). *Mechanics of Solid Materials*. Cambridge: Cambridge University Press.

Lewis, E., and Wallace, D. W. R. (1998). *Program Developed for CO2 System Calculations*. Silver Spring, MD: NOAA.

Lunden, J. J., McNicholl, C. G., Sears, C. R., Morrison, C. L., and Cordes, E. E. (2014). Acute survivorship of the deep-sea coral Lophelia pertusa from the Gulf of Mexico under acidification, warming, and deoxygenation. *Front. Mar. Sci.* 1:78.

McCulloch, M., Falter, J., Trotter, J., and Montagna, P. (2012a). Coral resilience to ocean acidification and global warming through pH up-regulation. *Nat. Clim. Chang.* 2, 623–633. doi: 10.1038/nclimate1473

McCulloch, M., Trotter, J., Montagna, P., Falter, J., Dunbar, R., Freiwald, A., et al. (2012b). Resilience of cold-water scleractinian corals to ocean acidification: Boron isotopic systematics of pH and saturation state up-regulation. *Geochim. Cosmochim. Acta* 87, 21–34. doi: 10.1016/j.gca.2012.03.027

Mirzaali, M., Bürki, A., Schwiedrzik, J. J., Zysset, P. K., and Wolfram, U. (2015). Continuum damage interactions between tension and compression in osteonal bone. *J. Mech. Behav. Biomed.* 49, 355–369. doi: 10.1016/j.jmbbm.2015.05.007

Mirzaali, M., Schwiedrzik, J. J., Thaiwichai, S., Best, J., Michler, J., Zysset, P. K., et al. (2016). Mechanical properties of cortical bone and their relationships with age, gender, composition and microindentation properties in the elderly. *Bone* 93, 196–211. doi: 10.1016/j.bone.2015.11.018

Mollica, N. R., Guo, W., Cohen, A. L., Huang, K.-F., Foster, G. L., Donald, H. K., et al. (2018). Ocean acidification affects coral growth by reducing skeletal density. *Proc. Natl. Acad. Sci. U.S.A.* 115, 1754–1759. doi: 10.1073/pnas.1712806115

Movilla, J., Gori, A., Calvo, E., Orejas, C., Lopez-Sanz, A., Dominguez-Carrio, C., et al. (2014). Resistance of two Mediterranean cold-water coral species to low-pH conditions. *Water* 6, 59–67. doi: 10.3390/W6010059

Oliphant, T. E. (2007). Python for scientific computing. *Comput. Sci. Eng.* 9, 10–20.

Osborne, E. B., Thunell, R. C., Gruber, N., Feely, R. A., and Benitez-Nelson, C. R. (2019). Decadal variability in twentieth-century ocean acidification in the California Current Ecosystem. *Nat. Geosci.* 13, 42–49. doi: 10.1038/s41561-019-0499-z

Otsu, N. (1979). A threshold selection method from grey level histograms. *IEEE T. Syst. Man. Cybernet.* 9, 62–66. doi: 10.1109/tsmc.1979.4310076

Pasquini, L., Molinari, A., Fantazzini, P., Dauphen, Y., Cuif, J. P., Levy, O., et al. (2015). Isotropic microscale mechanical properties of coral skeletons. *J. R. Soc. Interface* 12:20150168. doi: 10.1098/rsif.2015.0168

Perez, F. F., Fontela, M., García-Ibáñez, M. I., Mercier, H., Velo, A., Lherminier, P., et al. (2018). Meridional overturning circulation conveys fast acidification to the deep Atlantic Ocean. *Nature* 554, 515–518. doi: 10.1038/nature25493

Purser, A., Larsson, A. I., Thomsen, L., and van Oevelen, D. (2010). The influence of flow velocity and food concentration on Lophelia pertusa (Scleractinia) zooplankton capture rates. *J. Exp. Mar. Bio. Ecol.* 395, 55–62. doi: 10.1016/j.jembe.2010.08.013

R Development Core Team (2008). *R: A Language and Environment for Statistical Computing*. Vienna: R Development Core Team.

Roberts, J. M., Wheeler, A., Freiwald, A., and Cairns, S. D. (2009). *Cold-water corals: The biology and geology of deep-sea coral habitats*. Cambridge: Cambridge University Press.

Roberts, J. M., Wheeler, A. J., and Freiwald, A. (2006). Reefs of the deep: the biology and geology of cold-water coral ecosystems. *Science* 312, 543–547. doi: 10.1126/science.1119861

Salgado, E. J., Nehasil, S. E., and Etnoyer, P. J. (2018). Distribution of deep-water corals, sponges, and demersal fisheries landings in Southern California,

USA: implications for conservation priorities. *PeerJ* 6:e5697. doi: 10.7717/peerj.5697

Sarma, V. V. S. S., Ono, T., and Saino, T. (2002). Increase of total alkalinity due to shoaling of aragonite saturation horizon in the Pacific and Indian Oceans: Influence of anthropogenic carbon inputs. *Geophys. Res. Lett.* 29:20. doi: 10.1029/2002GL015135

Schwiedrzik, J. J., Raghavan, R., Bürki, A., LeNader, V., Wolfram, U., Michler, J., et al. (2014). In situ micropillar compression reveals superior strength and ductility but an absence of damage in lamellar bone. *Nat. Mat.* 13, 740–747. doi: 10.1038/nmat3959

Scott, P. J. B., and Risk, M. J. (1988). The effect of Lithophaga (Bivalvia: Mytilidae) boreholes on the strength of the coral Porites lobata. *Coral Reefs* 7, 145–151. doi: 10.1007/BF00300974

Secretariat of the Convention on Biological Diversity [CBD] (2014). *An Updated Synthesis of the Impacts of Ocean Acidification on Marine Biodiversity*, eds S. J. Hennige, J. M. Roberts, and P. Williamson (Montreal QC: Secretariat of the Convention on Biological Diversity).

Shaw, E. C., McNeil, B. I., and Tilbrook, B. (2012). Impacts of ocean acidification in naturally variable coral reef flat ecosystems. *J. Geophys. Res. Ocean.* 117:C03038. doi: 10.1029/2011JC007655

Spiesz, E. M., Roschger, P., and Zysset, P. K. (2012). Elastic anisotropy of uniaxial mineralized collagen fibers measured using two-directional indentation. Effects of hydration state and indentation depth. *J. Mech. Behav. Biomed. Mater.* 12, 20–28. doi: 10.1016/j.jmbbm.2012.03.004

Swartz, J. (1962). *Some Physical Constants for the Marshall Island Area. Geological Survey professional paper*; 260-AA. Washington, DC: United States Government Printing Office.

Thresher, R. E., Tilbrook, B., Fallon, S., Wilson, N. C., and Adkins, J. (2011). Effects of chronic low carbonate saturation levels on the distribution, growth and skeletal chemistry of deep-sea corals and other seamount megabenthos. *Mar. Ecol. Prog. Ser.* 442, 87–99. doi: 10.3354/meps09400

Titschack, J., Fink, H. G., Baum, D., Wienberg, C., Hebbeln, D., and Freiwald, A. (2016). Mediterranean cold water corals - an important regional carbonate factory? *Depos. Rec.* 2, 74–96. doi: 10.1002/dep2.14

Tunnicliffe, V. (1979). "The role of boring sponges in coral fracture," in *Biologie des Spongiares*, eds C. Levi and N. Boury-Esnault (Paris: Centre National de la Recherche Scientifique), 309–315.

Tunnicliffe, V. (1981). Breakage and propagation of the stony coral Acropora cervicornis. *Proc. Natl. Acad. Sci. U.S.A.* 78, 2427–2431. doi: 10.1073/pnas.78.4.2427

Vad, J., Orejas, C., Moreno-Navas, J., Findlay, H. S., and Roberts, J. M. (2017). Assessing the living and dead proportions of cold-water coral colonies: implications for deep-water Marine Protected Area monitoring in a changing ocean. *PeerJ* 5:e3705. doi: 10.7717/peerj.3705

van Aarle, W., Palenstijn, W. J., Cant, J., Janssens, E., Bleichrodt, F., Dabravolski, A., et al. (2016). Fast and flexible X-ray tomography using the ASTRA toolbox. *Opt. Express.* 24, 25129–25147. doi: 10.1364/OE.24.025129

van Aarle, W., Palenstijn, W. J., De Beenhouwer, J., Altantzis, T., Bals, S., Batenburg, K. J., et al. (2015). The ASTRA Toolbox: A platform for advanced algorithm development in electron tomography. *Ultramicroscopy* 157, 53–47. doi: 10.1016/j.ultramic.2015.05.002

van der Walt, S., Schönberger, J. L., Nunez-Iglesias, J., Boulogne, F., Warner, J. D., Yager, N., et al. (2014). Scikit-image: Image processing in Python. *PeerJ* 2:e453. doi: 10.7717/peerj.453

Wadeson, N., and Basham, M. (2016). Savu: A Python-based, MPI framework for simultaneous processing of multiple, N-dimensional, large tomography datasets. *arXiv [Preprint]* Available online at: https://arxiv.org/ftp/arxiv/papers/1610/1610.08015.pdf (accessed December 3, 2018).

Wilson, J. B. (1979). Patch development of the deep-water coral Lophelia pertusa on Rockall Bank. *J. Mar. Biol. Assoc. United Kingdom.* 59, 165–177. doi: 10.1017/S0025315400046257

Wisshak, M., Schoenberg, C. H. L., Form, A., and Freiwald, A. (2012). Ocean acidification accelerates reef bioerosion. *PLoS One* 7:e45124. doi: 10.1371/journal.pone.0045124

Wolfram, U., Gross, T., Pahr, D., Schwiedrzik, J. J., Wilke, H.-J., and Zysset, P. K. (2012). Fabric based Tsai-Wu yield criteria for vertebral trabecular bone in stress

and strain space. *J. Mech. Behav. Biomed.* 15, 218–228. doi: 10.1016/j.jmbbm. 2012.07.005

Wolfram, U., Wilke, H.-J., and Zysset, P. K. (2010). Rehydration of vertebral trabecular bone: influences on its anisotropy, its stiffness and the indentation work with a view to age, gender and vertebral level. *Bone* 46, 348–354. doi: 10.1016/j.bone.2009.09.035

Yoklavich, M., Laidig, T., Krigsman, L., Taylor, A., Watters, D., Love, D., et al. (2011). "A characterization of the coral and sponge community on Piggy Bank seamount in Southern California from a survey using a remotely operated vehicle," in *Proceedings of the A Report to NOAA Deep-Sea Coral Research and Technology Program* (Silver Spring, MD: NOAA).

Yoklavich, M. M., Love, M. S., and Forney, K. A. (2007). A fishery-independent assessment of an overfished rockfish stock, cowcod (Sebastes levis), using direct observations from an occupied submersible. *Can. J. Fish. Aquat. Sci.* 64, 1795–1804. doi: 10.1139/f07-145